CRYSTAL GROWTH & DESIGN

Article

Cite This: Cryst. Growth Des. XXXX, XXX, XXX-XXX

pubs.acs.org/crystal

Iron Sulfide Formation on Iron Substrates by Electrochemical Reaction in Anoxic Conditions

Xiaofei Guan,[†,‡,#] Brandon C. Enalls,[‡] David R. Clarke,[*,†] and Peter Girguis[*,‡]

[†]John A. Paulson School of Engineering and Applied Sciences and [‡]Department of Organismic & Evolutionary Biology, Harvard University, Cambridge, Massachusetts 02138, United States

Supporting Information

ABSTRACT: Electrodeposition has been widely used for the low-cost formation of large-area thin films of various crystalline materials. In this work, we use thermodynamic calculations to guide electrochemical experiments, in which we conduct a systematic investigation of crystalline iron sulfides formation on electrically poised iron substrates in H_2S aqueous solutions. Whereas thermodynamic calculations predict the formation of iron pyrite (FeS_2) films at the conditions tested, the principal iron−sulfur mineral phases observed were mixtures of mackinawite ($Fe_{1+x}S$) and cubic iron sulfide (phase identification and characterization included X-ray diffraction, Raman spectroscopy, scanning electron microscopy, and transmission electron microscopy). These data suggest that the phases formed are determined kinetically, not thermodynamically, across all tested electrodeposition conditions. The results are compared with the formation of iron sulfides produced by the "sour corrosion" of iron and steels, and in addition the effects of the experimental variables on the formation and morphologies of crystalline iron sulfides are discussed.

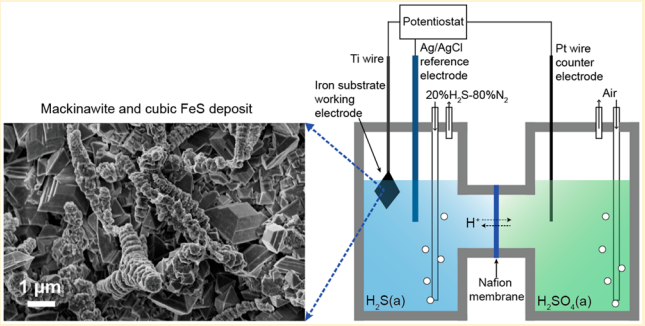

1. INTRODUCTION

Iron and sulfur are among the most abundant elements in Earth's crust. Their elemental cycles are closely linked biogeochemical processes with iron sulfides especially iron pyrite (cubic FeS_2) as the major sink for sulfur in various anoxic environments (e.g., freshwater and marine sediments, hydrothermal vents).[1,2] In addition, from the perspective of materials science, iron pyrite has been identified as a promising candidate solar absorber for photovoltaic solar cells based on the combination of several attractive characteristics.[3−5] For instance, it has a high optical absorption coefficient ($\alpha \geq 6 \times 10^5$ cm $^{-1}$) in the visible region,[3] a band gap of 0.95 eV,[3] and a long minority carrier diffusion length (0.1−1 μm),[6] key characteristics for solar energy absorbers. Also, unlike many more exotic semiconductors, such as CdTe, GaAs, and $Cu(In_xGa_{1-x})Se_2$,[7] its constituent elements are not only distributed widely geographically around the Earth but the compound is not toxic.

In its mineral form, iron pyrite is typically found in low-temperature anoxic sedimentary environments where it is believed that most of the free hydrogen sulfide (H_2S) is produced by the activity of sulfate-reducing microorganisms.[8] Pyrite nanoparticles can also be formed in aqueous solutions under a variety of anoxic conditions in the presence of H_2S.[8] While the detailed microbial mechanisms for the formation of iron pyrite are still far from clear, a variety of different iron sulfide polymorphs have been reported to occur.[8−11]

In contrast to the biogenic formation of iron pyrite, its formation during metal corrosion is much better understood, including the conditions under which nonstoichiometric compounds form. This knowledge is largely due to the widespread use of steel pipes in the petroleum industry to transport crude oil and gas. Raw hydrocarbon fuels contain water and H_2S that promote corrosion, which is often referred to as "sour corrosion". Whereas much research has been conducted on corrosion and approaches to ameliorate corrosive reactions, knowledge regarding the reaction pathways and the properties (e.g., crystalline structure, morphology, stoichiometry, electronic structure) of iron sulfides as corrosion products is still inadequate.[12−14] This is largely due to the complexity of this type of corrosion reaction, which depends on particular materials being affected as well as environmental factors. Specifically, materials factors can include matrix composition, lattice structure, crystalline defect, crystal orientation, grain size, impurity level, and surface state of iron or steels.[15] Environmental factors typically include temperature, pressure, flow velocity, H_2S concentration, CO_2 concentration, exposure time, electrical potential, pH level, and the presence of any sulfate-reducing biofilms.[12,16−27] In addition, the iron−sulfur chemistry is particularly complex in low temperature environments,[1,28] since at least nine distinct crystalline phases of varying

Received: July 21, 2017
Revised: October 23, 2017
Published: November 13, 2017

DOI: 10.1021/acs.cgd.7b01013
Cryst. Growth Des. XXXX, XXX, XXX−XXX

stoichiometries and stabilities can form: mackinawite (tetragonal $Fe_{1+x}S$, $0 \le x \le 0.11$), cubic FeS (sphalerite-like structure), troilite (hexagonal FeS), pyrrhotite (hexagonal or monoclinic $Fe_{1-x}S$, $0 \le x \le 0.17$), smythite (hexagonal $Fe_{3+x}S_4$, $0 \le x \le 0.3$), greigite (cubic Fe_3S_4), ferric sulfide (Fe_2S_3, unstable above 20 °C),[29] marcasite (orthorhombic FeS_2), and iron pyrite (cubic FeS_2). Among these, the main sulfides that form and are associated with H_2S-triggered corrosion of pure iron or steels are mackinawite, pyrrhotite, troilite, and iron pyrite.[14,30]

Perhaps the best understood is the formation of mackinawite. It has been reported as an initial corrosion product under most conditions in which steels are exposed in H_2S-bearing solutions in low-temperature ranges (below 100 °C).[14,31−33] For example, Smith et al. have discussed an empirical picture of the multistage sour corrosion mechanism with mackinawite formation as the first step. As the mackinawite grows to a critical thickness, it ruptures, and a second stage of mackinawite film growth takes place during which other more stable Fe−S phases such as pyrrhotite, troilite, and iron pyrite can nucleate and grow.[32] Shoesmith et al. have also reported electrochemical formation of mackinawite on iron in alkaline sulfide solutions.[34] It is also noted that in some work on corrosion of iron or carbon steel by H_2S-saturated water, mackinawite emerged as an initial corrosion product along with some rarer sulfides such as cubic FeS and troilite.[24,35]

Despite numerous research and field studies on sour corrosion of iron and steels, there is limited systematic experimental work exploring the conditions at which particular reaction products form as well as the underlying mechanisms by which H_2S triggers corrosion. Also, little is known about the exact role of temperature, time, and electrical potential on the morphology and crystalline structure of the initial reaction products (especially at relatively low temperatures). The purpose of this study is to systematically investigate the formation of thin-film crystalline iron sulfides on iron substrates submerged in H_2S-containing solutions. This detailed examination leads to an improved mechanistic understanding of iron sulfide chemistry during the H_2S-triggered corrosion process and advances our understanding of the (electro)chemical relationships between iron, sulfur, and other elements.

2. EXPERIMENTAL SECTION

A. Electrochemical Reactor. Figure 1 shows the schematic of the electrochemical reactor used for the experiments. It consisted of two borosilicate glass bottles, each equipped with flanged side arms that allow two bottles to be held together by a vacuum clamp (Adams and Chittenden Scientific Glass, CA, USA). Butyl rubber stoppers were used to cover the top openings of the two compartments. The two bottles were separated by a Nafion 117 polymer electrolyte membrane (Fuel Cell Store, TX, USA), which acts to separate the liquid electrolytes in each of the bottles. One compartment contained a 2 mM H_2S aqueous solution prepared by successively adding 72 mg of $Na_2S{\cdot}9H_2O$ (Alfa Aesar, MA, USA) and 16 μL of concentrated H_2SO_4 (Sigma-Aldrich, MO, USA) to 150 mL of ultrapure water (ELGA PURELAB flex, UK) deoxygenated by sparging with N_2. A 99.5% pure iron substrate (Goodfellows, PA, USA) with a surface area of ~2 cm^2 served as a working electrode. The iron substrate was polished by mounting in epoxy, and each side was polished progressively by using SiC sandpapers from P320 to P4000 grits and then using cloths with 6 μm, 3 μm, 1 μm diamond suspension and 0.05 μm alumina suspension. The polished iron substrate was separated from the epoxy and further cleaned using acetone, ethanol, and ultrapure water. Next, a titanium wire was coupled to the iron coupon using silver-impregnated epoxy that was baked at 50 °C for 12 h. This connection was then covered entirely by silicone epoxy. A custom-made silver/

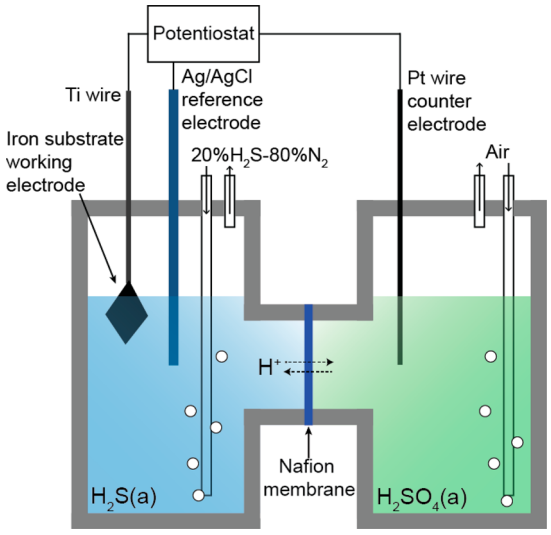

Figure 1. Schematic of the electrochemical cell with a typical three-electrode arrangement consisting of an iron substrate as the working electrode, a Ag/AgCl reference electrode, and a Pt wire as the counter electrode.

silver chloride (Ag/AgCl) system served as a reference electrode consisting of an internal Ag wire with AgCl deposited on its surface, and an internal filling solution of 3 M KCl saturated with AgCl (Microelectrodes Inc., NH, USA). During the experiments, both the iron substrate working electrode and the Ag/AgCl reference electrode were immersed in the solution. A 20%H_2S−80%N_2 gas mix was flowed into the solution at a rate of ~10 cm^3/min. This maintained a relatively constant level of soluble H_2S as well as anaerobicity. The gas flowing also helped improve the homogeneity of the solution regarding pH distribution. The second compartment contained a Pt wire counter electrode that was submerged ~4 cm deep into a 150 mL 2 mM H_2SO_4 aqueous solution. The H_2SO_4 solution was open to air and was bubbled constantly using an aquarium pump to maintain oxygen saturation. All experiments were run at either 20 or 65 °C. For the experiments at 65 °C, the electrochemical reactor was heated in a bead bath (Lab Armor, OR, USA). The bulk pH levels of the liquid electrolytes in the working electrode compartment were measured right before and after experiments by using a double junction pH probe (Mettler Toledo, OH, USA). Given the high toxicity of H_2S gas, all the experiments involving H_2S were performed inside a fume hood.[36]

B. Determining Aqueous H_2S Concentrations. Because the aqueous H_2S concentration is an important experimental variable for iron sulfide synthesis, solutions bubbled with 20%H_2S−80%N_2 at both 20 and 65 °C were sampled for H_2S analyses via a spectrometric assay by Cline.[37] Briefly, using a syringe flushed with N_2, 0.1 mL aliquots were taken and fixed in 2.9 mL of a solution containing 91 mM zinc acetate and 3.48 mM acetic acid dissolved in ultrapure H_2O. Afterward, the samples were stored at −20 °C until the assay was performed. Upon defrosting, 0.05 mL of the fixed sample was added to 1 mL of the 91 mM zinc acetate solution, followed by the subsequent additions of 3.425 mL of ultrapure H_2O (made anoxic by boiling and sparging with N_2 gas during cooling), 0.5 mL of 0.2% *n,n*-dimethyl-*p*-phenylenediamine sulfate dissolved in 2.5 M H_2SO_4, and 0.025 mL of 1% ferric ammonium sulfate suspended in 368 mM H_2SO_4. Samples were vortexed and allowed to sit for at least 1 h to allow for the color changing reaction to occur completely before transferring 1 mL to a cuvette for spectrophotometric analysis. Absorbance was read at 670 nm using a Cary 100 UV/vis spectrophotometer (Agilent Technologies). Absorbance was converted to concentration of dissolved sulfide in mM using a standard curve generated from known concentrations of sodium sulfide nonahydrate dissolved in anoxic ultrapure H_2O (ranging from 2 mM down to 0.05 mM). Unlike the unknown samples, 0.05 mL aliquots of these standard dilutions

DOI: 10.1021/acs.cgd.7b01013
Cryst. Growth Des. XXXX, XXX, XXX−XXX

were used directly in the assay without first being fixed in the zinc acetate and acetic acid solution.

C. Electrochemical Measurements. To electrochemically characterize the working electrode, open circuit voltage (OCV) measurements, cyclic voltammetry (CV) scans, electrochemical impedance spectroscopy (EIS) scans, and controlled potential (CP) measurements and scans were performed using a Gamry Interface 1000 potentiostat (Gamry, PA, USA). All electrode potentials in this paper are reported relative to the Ag/AgCl reference electrode unless stated otherwise. The OCV measurements recorded the voltage of the iron substrate working electrode vs the Ag/AgCl reference electrode under open circuit condition. The CV measurements were carried out to study the interaction between the iron substrate and the H_2S aqueous solution within the electrical potential window (−1.5 V − 1 V) at a scan rate of 100 mV s^{-1}. EIS scans were conducted to characterize the resistances involved in the cell under open circuit condition from 10 000 to 1 Hz with sinusoidal perturbation of 20 mV amplitude. At CP scans the iron substrate working electrodes were poised at different potentials (−0.8 ,−0.2, and 0.2 V) vs the Ag/AgCl reference electrode for electrodeposition, current response, and total charge passed were recorded with time. In control experiments, the iron substrate was tested in the same chemical environment except that no voltage was applied (i.e., open circuit condition).

D. Materials Characterization. A Bruker D2 phaser X-ray diffractometer with a copper target and a conventional θ-2θ diffraction geometry was used to determine the crystalline phase of the deposits and the substrates. X-ray diffraction (XRD) patterns were collected within a range of the diffraction angle 2θ from 10° to 80° in steps of 0.02°, and an integration time of 1 s per step. The Powder Diffraction File (PDF) card database was used as the reference for crystalline phase identification.[38] Field-emission scanning electron microscopy (SEM; Zeiss Supra) was used to investigate the surface morphologies. To examine the cross sections of the iron substrate samples, they were impregnated with epoxy resin and hardener (West System, MI, USA). After the epoxy hardened, the samples were polished by using SiC sandpapers from P320 to P4000 grits, and then coated with a 5 nm Pt/Pd layer (Quorum Technologies, UK) for SEM imaging. Raman spectra on the films were recorded using LabRAM Aramis Raman system (Horiba Jobin Yvon) with laser excitation at 532 nm. The Raman spectra were collected within a range of the Raman shift from 200 to 475 cm^{-1} (with ×10 objective lens and ×1800 grating). A ~100 nm thick lamella was prepared from a bulk specimen using lift-out technique in a focused ion beam (FIB) system (FEI Helios Nanolab 660). The lamella was then examined in a transmission electron microscope (TEM; JEOL 2100) to acquire selective area electron diffraction (SAED) patterns.

3. THERMODYNAMIC CALCULATION OF THE POURBAIX DIAGRAM

To guide the electrochemical experiments and predict the thermodynamic stability of different iron sulfides in aqueous solution, a Pourbaix diagram was constructed for the Fe−S−H_2O system at both 20 and 65 °C and 1 atm total pressure using the HSC Chemistry database.[39] The thermodynamic data of 44 chemical species consisting of chemical elements (Fe, S, H, and/or O) in liquid, condensed, and aqueous phases were considered (see Note S1). The Pourbaix diagrams in Figure 2 depict the conditions for the thermodynamic stability of different iron sulfides, including iron pyrite (FeS_2), pyrrhotite ($Fe_{0.877}S$), and mackinawite (FeS) in aqueous solution, as a function of electrode potential and pH. The regions over which iron pyrite is the predominant stable species are highlighted on both diagrams. Pourbaix diagrams, such as these, do not take kinetic effects into account. The actual experimental results are reported in the following section.

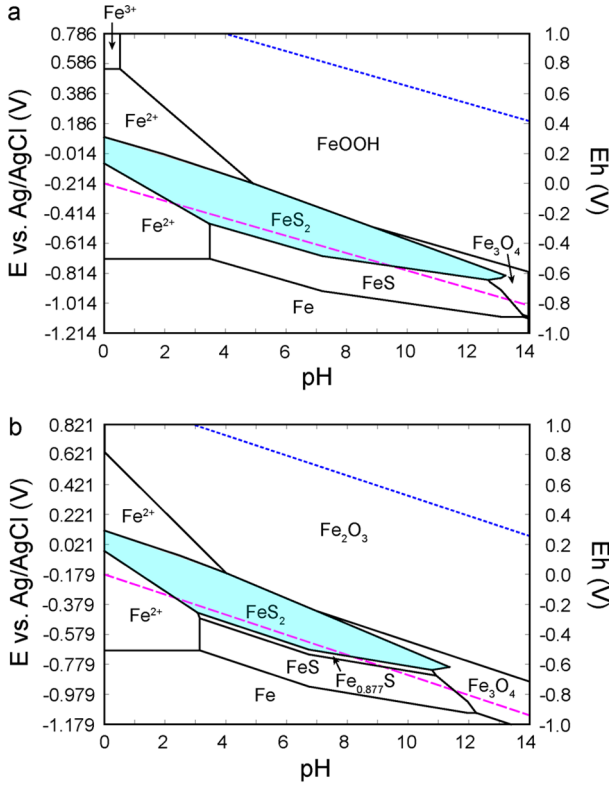

Figure 2. Pourbaix diagrams of the Fe−S−H_2O system at 20 °C (a) and 65 °C (b). The molarity of elements Fe and S were set to 100 mM and 2 mM to simulate the actual experimental system. The upper and lower stability limits of water are shown in both diagrams with blue dotted and cyan dashed lines, respectively. *E* vs Ag/AgCl is equal to Eh - 0.214 V at 20 °C and Eh - 0.179 V at 65 °C (see Note S2), where Eh is the potential vs standard hydrogen electrode (SHE).

4. RESULTS AND DISCUSSION

The electrodeposition experimental setup (Figure 1) was used to investigate the nature and extent of iron sulfide deposition on poised zerovalent iron surfaces. The iron substrates were subjected to a range of experimental conditions as outlined in Table 1, to study the dependence of the reaction products on electrode potential (E), temperature (T), and duration (t).

The corrosion potential of the iron substrate working electrode is a steady-state potential determined kinetically by equating the rates of all oxidation and reduction processes in the absence of electrical connections.[40] It was determined to be approximately −0.6 V at both 20 and 65 °C by measuring the open circuit voltage between the working electrode potential and the Ag/AgCl reference electrode. A more oxidizing potential (e.g., −0.2 V, 0.2 V) was then applied to the working electrode to drive the half reaction ($Fe^{2+} + 2e^- = Fe$) toward Fe^{2+} formation at the iron substrate/H_2S aqueous solution interface. The pH of the solution in the working electrode compartment selected for the experiments (Table 1) ranged from 2.7 to 4.4. We selected acidic conditions so that $H_2S(a)$, not the S^{2-} or HS^-, was the dominating sulfur species.[41] The underlying concept being that, as Fe is oxidized to Fe^{2+}, it reacts with $H_2S(a)$ present at the interface, leading to the deposition of iron sulfides on the iron substrate.

Table 1 shows that the pH of the $H_2S(a)$ solution shift slightly over each experiment, which can be attributed to multiple factors. For example, the direct reaction between iron and H^+ ($Fe + H^+ \rightarrow Fe^{2+} + H_2(g)$) consumes H^+ and thereby

DOI: 10.1021/acs.cgd.7b01013
Cryst. Growth Des. XXXX, XXX, XXX−XXX

Table 1. Experimental Details for the Iron Substrate Samples II–VIII[a]

sample label	E (V)	T (°C)	t (h)	Q (C)	pH of the H_2S(a) solution: initial pH	pH of the H_2S(a) solution: final pH
II	unpolarized	20	24	0	3.1	3.4
III	−0.2	20	24	86	3.4	3.3
IV	unpolarized	65	24	0	3.1	4.4
V	−0.2	65	24	147	3.5	4.3
VI	0.2	65	24	399	3.5	4.1
VII	−0.8	65	24	−110	3.2	2.7
VIII	−0.2	65	90	1005	3.5	3.8

[a]Sample I was a pristine iron substrate and therefore was not included. The samples II–VIII were subjected to free corrosion under open circuit condition or an electrical potential (−0.8 V, −0.2 V, or 0.2 V) for different periods of time (24 or 90 h) at different temperatures (20 or 65 °C). The potentials of the unpolarized iron substrate samples II and IV under open circuit condition were measured to be approximately −0.6 V vs. Ag/AgCl.

leads to a local pH increase. In addition, the charge transfer reactions involving H^+ at both electrodes and the diffusion of H^+ and water across the Nafion membrane affect the pH level as well. While it is difficult to keep the pH at a constant value, it is noted that, within this pH range, iron pyrite is predicted to be the thermodynamically favorable phase at some slightly oxidizing potentials (e.g., −0.2 V vs Ag/AgCl) at both 20 and 65 °C according to the Pourbaix diagrams (Figure 2).

Nyquist plots of the initial cell impedance data obtained are shown in Figure 3a,b. The high-frequency intercept of the impedance data with the real axis gives the ohmic resistance, which includes the ohmic resistance of the iron substrate, the liquid electrolytes in both compartments, the polymer electrolyte membrane, the external lead wires, and the contact resistance associated with all interfaces. The nonohmic polarization resistance can be extrapolated from the difference between the high-frequency intercept and the low-frequency intercept with the real axis, and it is a measure of the reaction kinetics and diffusion of reactants near the electrodes. The sum of the ohmic resistance and the nonohmic polarization resistance is the total cell resistance. The cell operated at 20 °C showed an ohmic resistance of 416 Ω and a nonohmic polarization resistance of 121 Ω, while the cell operated at 65 °C showed lower ohmic resistance (192 Ω) and nonohmic polarization resistance (38 Ω). The difference in nonohmic polarization resistance verifies that the iron substrate in the system has a lower corrosion resistance at 65 °C than at 20 °C, although the solubility of H_2S in water also decreases with increasing temperature (Figure S1).[42]

The initial cyclic voltammograms obtained for iron as the working electrode immersed in the H_2S(a) solution operated at 20 and 65 °C (Figure 3c) reveal that the total resistance of the cell in steady state can be estimated from the inverse of the slope of the plot near the region of zero current. The greater slope of the plot at 65 °C than that at 20 °C corresponds to a smaller cell resistance, consistent with the aforementioned impedance results. The cyclic voltammograms are featureless and do not exhibit any hysteresis or pronounced redox peaks. This is likely attributed to the redox couple (Fe/Fe^{2+}) in this system, being distinct from redox couple present in solution as ions at an inert working electrode in typical electrochemical systems. Instead, it is concluded that Fe comes from the solid iron substrate so there was no mass transfer limitation behavior during anodic scan from −1.5 to 1 V, and consequently no obvious oxidation peak. In addition, there was no Fe^{2+} present in the initial solution, and any Fe^{2+} formed reacts immediately with H_2S(a) to form solid iron sulfide deposit on the iron substrate. This explanation is consistent with the absence of any identifiable reduction peak.

Following the initial electrochemical characterization, the iron substrate working electrodes were subjected to different potentials (i.e., −0.8 V, −0.2 V, 0.2 V) or free corrosion (i.e., open circuit potential) for different periods of time in different experiments. The working electrode potentials were set to mimic the presence of different redox reactions near iron in natural environment. Table 1 summarizes the experimental details including applied potential (E), temperature (T), duration (t), total charge passed (Q), as well as pH of the H_2S aqueous solution before and after experiments. After constant potential scans, the experimental setups were disassembled. The iron substrates were dipped and rinsed in ultrapure water to remove any soluble salt (Na_2S or Na_2SO_4) and then dried in an anaerobic environment inside an anaerobic glovebox before the characterization using XRD, Raman spectroscopy, SEM, and TEM.

Figure 4 shows the XRD patterns of the iron substrates after the experiments compared with that of the pristine iron substrate. The XRD pattern of the pristine iron substrate (labeled as sample I) shows two characteristic diffraction peaks

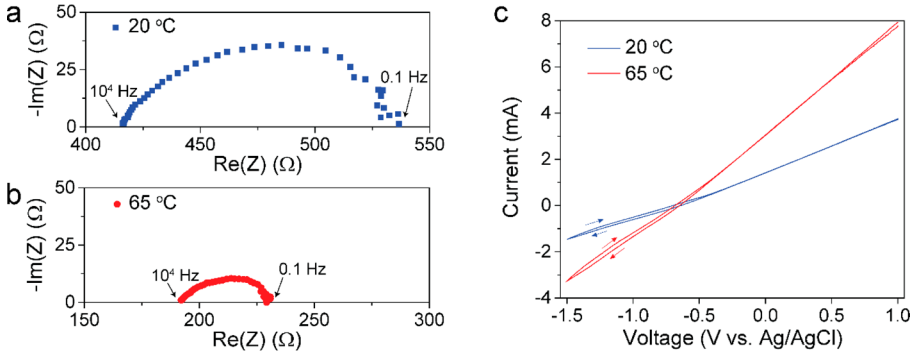

Figure 3. Initial electrochemical characterization results of the electrochemical cells. Nyquist plots of the initial EIS results of the cells at 20 °C (a) and 65 °C (b), respectively. (c) Initial cyclic voltammograms obtained for iron working electrode immersed in H_2S(a) solution of the electrochemical cells at 20 °C (blue line) and 65 °C (red line). The scans were recorded between 1 V and −1.5 V and started from the positive limit. Arrows indicate the scan direction. Scan rate: 100 mV/s.

DOI: 10.1021/acs.cgd.7b01013
Cryst. Growth Des. XXXX, XXX, XXX–XXX

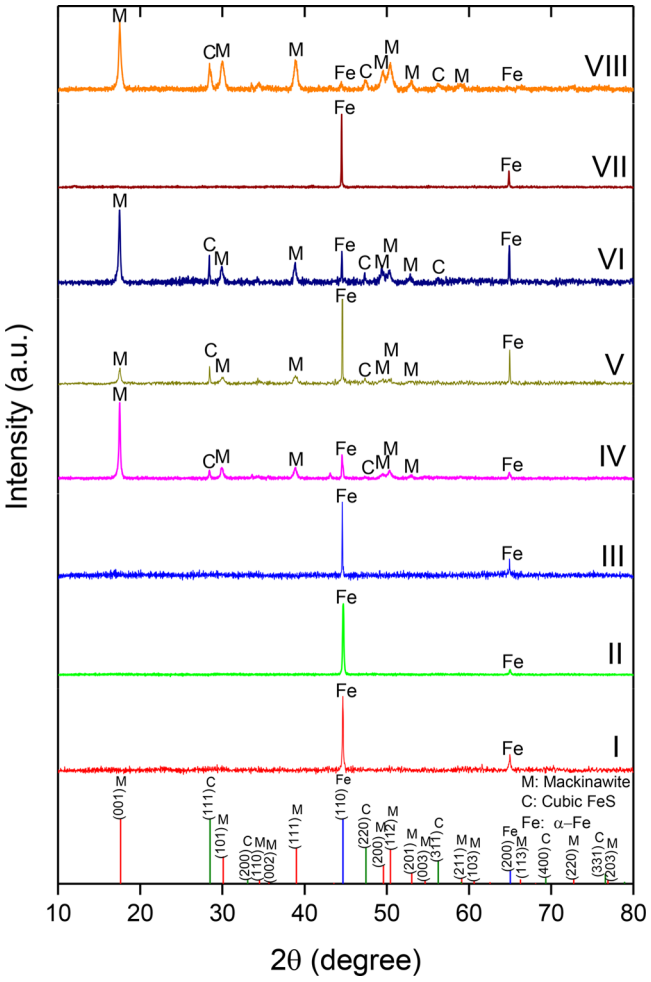

Figure 4. XRD patterns of the iron substrates after experiments. Sample I is a pristine iron substrate. Samples II–VIII were subjected to free corrosion or applied electrical potentials, and their experimental details are provided in Table 1. The letters M, C, and Fe in the XRD patterns indicate diffraction peaks of mackinawite (PDF card No. 01-086-0389), cubic FeS (PDF card No. 00-023-1123), and iron substrate (PDF card No. 00-006-0696), respectively. As references, the data sets from the standard PDF cards are plotted at the bottom panel.

at approximately 44.7° and 65° for α-iron with a body-centered cubic crystal structure (PDF card No. 00-006-0696). The XRD patterns of the iron substrates subjected to either free corrosion (Sample II) or electrical potential of -0.2 V (sample III) at 20 °C for 24 h did not show any additional diffraction peaks. In contrast, the XRD patterns of the iron substrates subjected to free corrosion (Sample IV), or electrical potentials of -0.2 V (Sample V) or 0.2 V (Sample VI) at a higher temperature (65 °C) for the same length of time show new diffraction peaks for mackinawite (tetragonal layer structure) and cubic FeS (sphalerite-like structure) in the deposits. The sharp, narrow peaks are indicative of good crystallinity. The absence of any measurable crystalline deposit on Samples II and III was attributed to the relatively low temperature as well as the short period of experimental time. Previously, it has been reported that it may take up to two years at 25 °C for initial amorphous iron sulfide precipitate to develop into well-crystallized mackinawite in aqueous solution without electrochemical polarization.[43] It is also understood that increasing the temperature accelerates the kinetics of transport phenomena as well as chemical and electrochemical reactions, facilitating the formation of these crystalline iron sulfides. In addition, the observation of cubic FeS is consistent with some findings in the literature. For instance, it has been reported that the cubic FeS is typically formed as a corrosion product of iron in H_2S aqueous solutions at a pH below 6 and temperatures below 92 °C at 1 bar total pressure.[44] However, in our experiments when an iron substrate (sample VII) was subjected to a reducing electrical potential (−0.8 V) at 65 °C for 24 h, no peaks for iron sulfides or oxides were observed by XRD. This is attributed to iron oxidation being prohibited at the reducing electrical potential below the corrosion potential. The anodic corrosion behavior of the iron substrate was also studied for an extended period, where an iron substrate (sample VIII) was poised at −0.2 V at 65 °C for 90 h. Under these conditions, strong diffraction peaks for both mackinawite and cubic FeS were observed, while simultaneously the iron diffraction peaks were substantially weakened because it was being corroded.

The crystalline deposits of Samples IV, V, VI, and VIII were further characterized by Raman spectroscopy (Figure 5). The

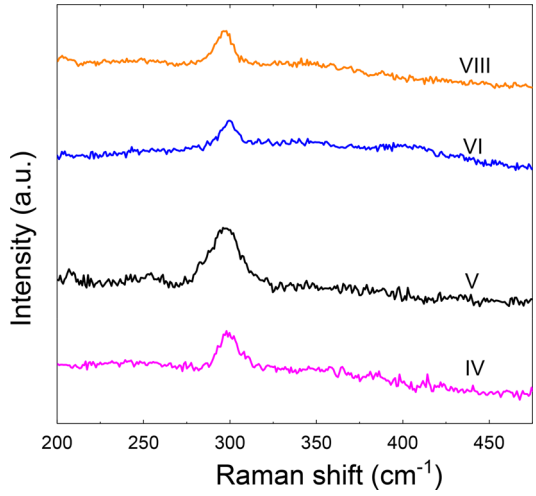

Figure 5. Raman spectra of samples IV, V, VI, and VIII. The experimental details for these samples are provided in Table 1.

spectra are all similar to a strong peak at ~300 cm^{-1} and a barely observable peak at ~250 cm^{-1}, characteristic peaks of mackinawite.[13,45] No Raman peaks attributable to cubic FeS can be identified from the measurements, although to the best of the authors' knowledge, neither experimental measurements nor theoretical modeling[46] of the Raman spectrum for cubic FeS is available in previous literature. Nevertheless, Osadchii et al. have reported on the Raman spectrum of sphalerite solid solution $Fe_{0.5}Zn_{0.5}S$ with a peak at ~300 cm^{-1} attributed to the presence of FeS groups and another peak at ~345 cm^{-1} attributed to ZnS groups.[47] This finding implies that the major Raman peak for pure cubic FeS is located at ~300 cm^{-1}, close to that of mackinawite. Therefore, the Raman peak identified in Figure 5 is likely contributed by both mackinawite and cubic FeS.

The as-polished pristine iron substrate (Sample I) has a smooth surface (Figure S2). The SEM images of Sample IV show a rough surface with irregular-shaped solids as a result of free corrosion of the iron substrate by H_2S (Figure 6a,b). In contrast, SEM images of Sample V that was poised at −0.2 V show well-faceted crystals as well as crystals with a roughly cylindrical aspect (Figure 6c–f). The well-faceted crystals

DOI: 10.1021/acs.cgd.7b01013
Cryst. Growth Des. XXXX, XXX, XXX−XXX

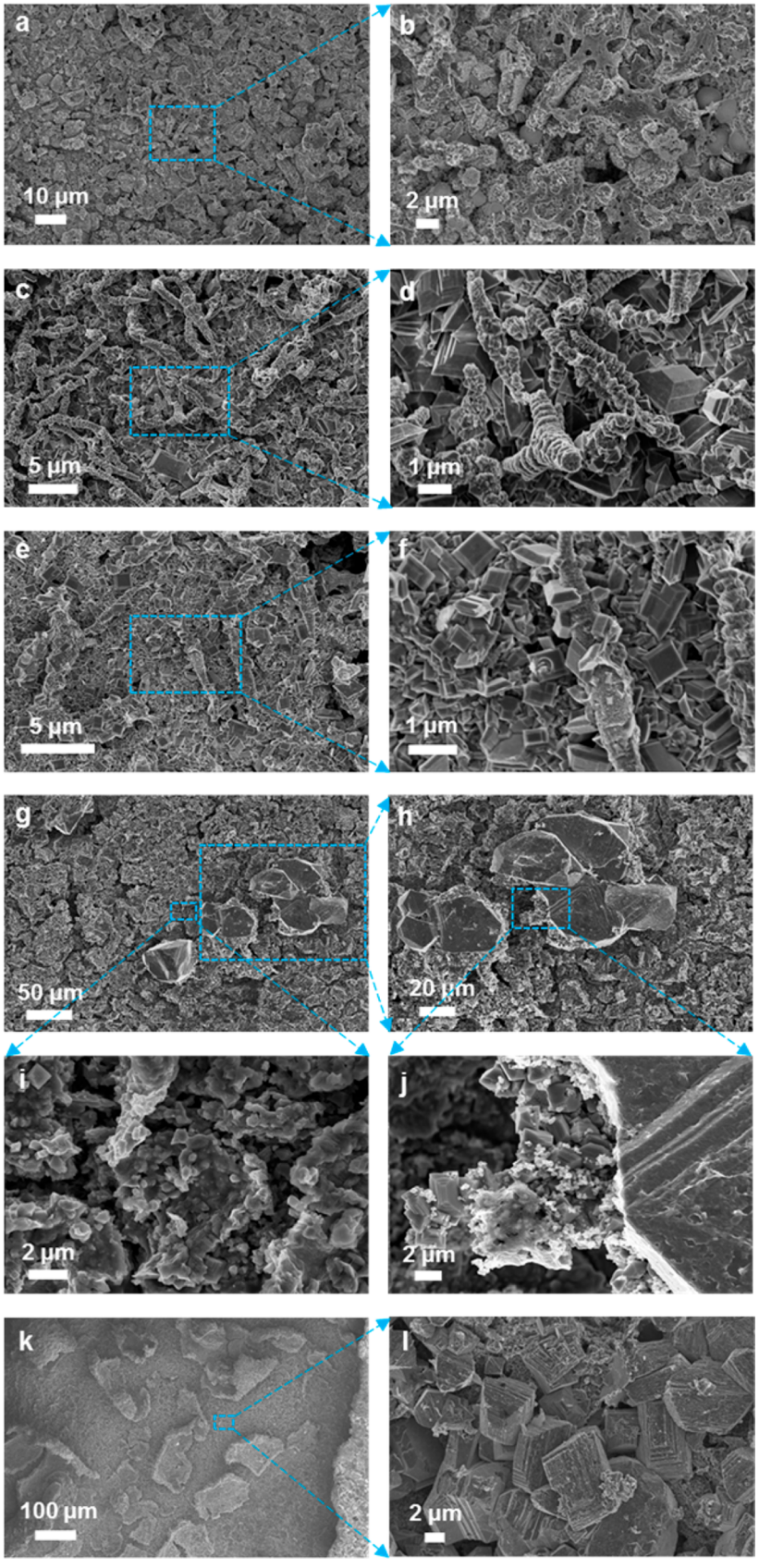

Figure 6. SEM images showing the surface morphology of the films formed on Samples IV (a, b), V (c–f), VI (g–j), and VIII (k, l).

typically have trapezoidal-shaped side faces and rectangle-shaped end faces. High-magnification SEM images of these crystals indicate a character of layer growth (Figure 6d,f).[48] An intergrowth of these two types of crystals are also observed (Figure 6f). SEM images of sample VIII that was poised at the same electrical potential but a long period of time (90 h) show

DOI: 10.1021/acs.cgd.7b01013
Cryst. Growth Des. XXXX, XXX, XXX–XXX

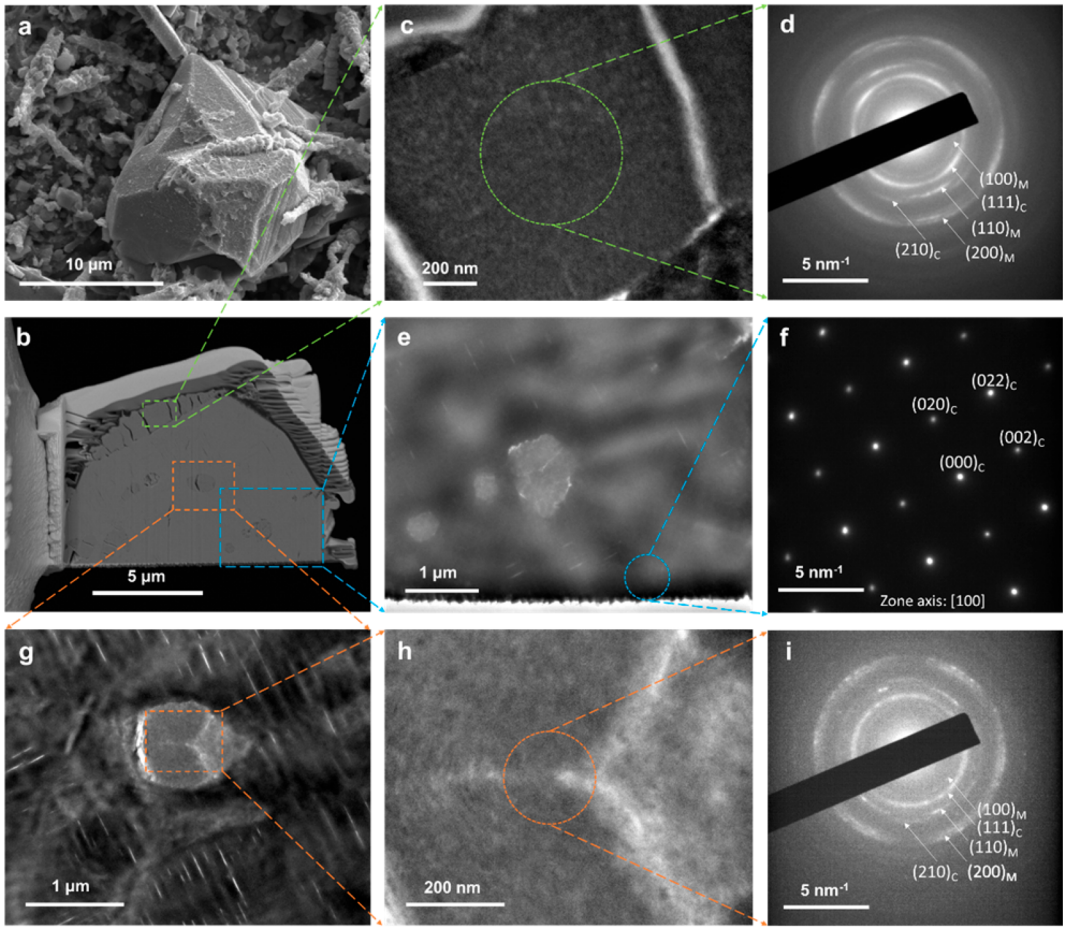

Figure 7. SEM, TEM images, and SAED patterns of the crystalline deposit on Sample V. (a) SEM image showing a large well-faceted crystal with a crystal of a roughly cylindrical aspect on the top. A lamella along the crystal of the roughly cylindrical aspect was removed from this bulk sample. (b) SEM image of the lamella for TEM studies. (c) TEM image of the crystal of the roughly cylindrical aspect enclosed inside the green square in (b). (d) SAED pattern for the selected area circled in (c) gives ring patterns, suggesting it a mixture of polycrystalline mackinawite and cubic FeS. (e) TEM image of the area enclosed in the blue square in (b). (f) SAED pattern for the area circled in (e), corresponding to monocrystalline cubic FeS. Zone axis: [100]. (g) TEM image of the area enclosed in the orange square in (b). (h) TEM image of the area enclosed in the orange square in (g). (i) SAED pattern for the area circled in (h), corresponding to a mixture of polycrystalline mackinawite and cubic FeS.

peeling on the surface, verifying that the iron substrate was seriously corroded (Figure 6k). High-magnification SEM image features the well-faceted crystals with a character of layer growth (Figure 6 l). SEM images of Sample VI that was poised at a more oxidizing potential (0.2 V) for 24 h show mixed morphologies featuring large crystal clusters (Figure 6g,h) and smaller well-faceted crystals (e.g., octahedron) (Figure 6i,j). The comparison between the SEM images of Sample IV, V, and VI implies that the application of electrical potential affects crystal morphology. The electrochemically driven phase formation processes for Sample V and VI involve a sequence of steps including the adsorption of H_2S onto the iron substrate accompanied by charge transfer reactions, and then the formation of iron sulfide nuclei and the growth of the new phase.[49] The applied potential maintains the supply of Fe^{2+} from the iron substrate to react with H_2S, more easily creating an oversaturation condition compared with the free corrosion. The cross-sectional view SEM images of the iron substrates mounted in epoxy show serious corrosion for Samples VI and VIII (Figure S3), consistent with the findings in Figure 7.

To differentiate the crystals on Sample V, a TEM lamella consisting of both phases was prepared from the bulk specimen, and SAED patterns for different areas on the lamella are shown in Figure 7. The SAED pattern of the crystal of the roughly cylindrical aspect gives rings suggesting a mixture of polycrystalline mackinawite and cubic FeS (Figure 7d). The SAED pattern of a smooth area of the well-faceted crystal shows single spots, corresponding to monocrystalline cubic FeS (Figure 7f). A survey of multiple spots shows similar SAED patterns, confirming that the well-faceted crystal is mostly cubic FeS. It is also noted that there are different phases embedded in the cubic FeS crystal (Figure 7b,g,h). The SAED pattern of one of these phases shows rings that also correspond to a mixture of polycrystalline mackinawite and cubic FeS. Figure 7b,c also shows an epitaxial growth of the crystal of the roughly cylindrical aspect on the well-faceted crystal. The coexistence and epitaxial nucleation and growth of cubic FeS on mackinawite are facilitated by their similarity in atomic arrangement as well as in lattice parameters.[24]

The most revealing finding of our studies is that, despite carrying out experiments at which iron pyrite phase is thermodynamically favored phase as predicted by the computed Pourbaix diagrams (Figure 2), only the metastable mackinawite and cubic FeS phases were observed to form. These data indicate that pyrite formation is kinetically limited, at least under the conditions investigated here. Similar experimental

DOI: 10.1021/acs.cgd.7b01013
Cryst. Growth Des. XXXX, XXX, XXX−XXX

conditions, but conducted at higher temperatures and/or higher pressures, may overcome kinetic barriers.[50] Nevertheless, these data provide a clear and repeatable glimpse into the process and extent of iron sulfide formation on electrically poised substrates, and underscore that a reliance on thermodynamic estimation (that do not take into account kinetics) can lead to inaccurate depictions of iron sulfide formation on surfaces in aqueous conditions.

5. CONCLUDING REMARKS

Herein, the electrochemical reaction of iron substrates in anoxic H_2S aqueous solution has been systematically studied with temperature, electrode potential and time. Crystalline mackinawite and cubic FeS but not iron pyrite were identified as the reaction products. The application of a more oxidizing potential leads to the formation of well-faceted crystals consisting of cubic FeS and mackinawite. We did not observe the formation of iron pyrite in sufficient abundance to detect with the instruments used here. This is of particular interest, as iron pyrite has been identified as a promising light absorber for photovoltaics. It remains a challenge to form iron pyrite thin film in aqueous solution by electrodeposition at low temperature (<100 °C) and ambient pressure. Further work is needed to exploit the advantages of electrodeposition technique in combination with other processes, such as high-temperature and high-pressure annealing, for the synthesis of iron pyrite thin films.

■ ASSOCIATED CONTENT

Supporting Information

The Supporting Information is available free of charge on the ACS Publications website at DOI: 10.1021/acs.cgd.7b01013.

Figure S1. H_2S contents in the aqueous solutions bubbled with 20%H_2S−80%N_2 at 20 and 65 °C. Table S1. Values of H_2S contents in the aqueous solutions bubbled with 20%H_2S−80%N_2 at 20 °C. Table S2. Values of H_2S contents in the aqueous solutions bubbled with 20%H_2S−80%N_2 at 65 °C. Note S1. A complete list of the chemical species consisting of chemical elements (Fe, S, H, and/or O) considered in the thermodynamic calculation of the Pourbaix diagrams. Note S2. Relationship between a potential E vs Ag/AgCl and Eh. Figure S2. (a) Plan-view SEM image of the as-polished pristine iron substrate. (b) Low-magnification and (c) high-magnification cross-sectional view SEM images of the as-polished pristine iron substrate. Figure S3. Low-magnification (left) and high-magnification (right) SEM images showing the cross-sectional view of iron substrates mounted in epoxies including Sample IV (a, b), V (c, d), VI (e, f), and VIII (g, h) (PDF)

■ AUTHOR INFORMATION

Corresponding Authors

*(D.R.C.) Address: 29 Oxford Street, Cambridge, MA 02138. Phone: 617-495-4140. E-mail: clarke@seas.harvard.edu. Web address: https://clarke.seas.harvard.edu/.

*(P.G.) Address: 16 Divinity Avenue, Cambridge, MA 02138, Phone: 617-496-8328. E-mail: pgirguis@oeb.harvard.edu. Web address: https://girguislab.oeb.harvard.edu/.

ORCID

Xiaofei Guan: 0000-0002-7100-2949

Present Address

#(X.G.) School of Physical Science and Technology, Shanghai Tech University, Shanghai 201210, China.

Notes

The authors declare no competing financial interest.

■ ACKNOWLEDGMENTS

Our work was funded by the Division of Materials Research and the Division of Ocean Sciences, National Science Foundation under the Award Number 1344241. The authors thank Dr. Aude Picard for helpful discussion. Part of the work was performed at the Center for Nanoscale Systems at Harvard University.

■ REFERENCES

(1) Rickard, D.; Schoonen, M. A. A.; Luther, G. W., III In *Geochemical Transformations of Sedimentary Sulfur;*; Vairavamurthy, M. A., Schoonen, M. A. A., Eglinton, T. I., Luther, G. W., III, Manowitz, B., Eds.; American Chemical Society: Washington, DC, 1995; Vol. *612*, Chapter 9, pp 168−193.

(2) Yucel, M.; Gartman, A.; Chan, C. S.; Luther, G. W. *Nat. Geosci.* **2011**, *4*, 367−371.

(3) Ennaoui, A.; Fiechter, S.; Goslowsky, H.; Tributsch, H. *J. Electrochem. Soc.* **1985**, *132*, 1579−1582.

(4) Ennaoui, A.; Fiechter, S.; Pettenkofer, Ch.; Alonso-Vante, N.; Buker, K.; Bronold, M.; Hopfner, Ch.; Tributsch, H. *Sol. Energy Mater. Sol. Cells* **1993**, *29*, 289−370.

(5) Puthussery, J.; Seefeld, S.; Berry, N.; Gibbs, M.; Law, M. *J. Am. Chem. Soc.* **2011**, *133*, 716−719.

(6) Ennaoui, A.; Tributsch, H. *Sol. Energy Mater.* **1986**, *14*, 461−474.

(7) Fthenakis, V. *MRS Bull.* **2012**, *37*, 425−430.

(8) Rickard, D. In *Sulfidic Sediments and Sedimentary Rocks*; Elsevier: Amsterdam, Netherlands, 2012; Chapter 6, pp 233−285.

(9) Picard, A.; Gartman, A.; Girguis, P. R. *Front. Earth Sci.* **2016**, *4*, Article 68, 1−10. DOI: 10.3389/feart.2016.00068

(10) Gramp, J. P.; Bigham, J. M.; Jones, F. S.; Tuovinen, O. H. *J. Hazard. Mater.* **2010**, *175*, 1062−1067.

(11) Pósfai, M.; Buseck, P. R.; Bazylinski, D. A.; Frankel, R. B. *Science* **1998**, *280*, 880−883.

(12) Genchev, G.; Cox, K.; Tran, T. H.; Sarfraz, A.; Bosch, C.; Spiegel, M.; Erbe, A. *Corros. Sci.* **2015**, *98*, 725−736.

(13) Genchev, G.; Erbe, A. *J. Electrochem. Soc.* **2016**, *163*, C333−C338.

(14) Sun, W.; Nesic, S. In *Corrosion Conference and Expo 2007*; NACE International: Houston, TX, 2007; Paper No. 07655, pp 1054−1079.

(15) Song, G.-L. *Front. Mater.* **2014**, *1*, Article 2, 1−3.

(16) Nešić, S. *Corros. Sci.* **2007**, *49*, 4308−4338.

(17) Wiener, M. S.; Salas, B. V.; Quintero-Núñez, M.; Zlatev, R. *Corros. Eng., Sci. Technol.* **2006**, *41*, 221−227.

(18) Banaś, J.; Lelek-Borkowska, U.; Mazurkiewicz, B.; Solarski, W. *Electrochim. Acta* **2007**, *52*, 5704−5714.

(19) Sosa, E.; Cabrera-Sierra, R.; García, I.; Oropeza, M. T.; González, I. *Corros. Sci.* **2002**, *44*, 1515−1528.

(20) Ma, H.; Cheng, X.; Li, G.; Chen, S.; Quan, Z.; Zhao, S.; Niu, L. *Corros. Sci.* **2000**, *42*, 1669−1683.

(21) Venzlaff, H.; Enning, D.; Srinivasan, J.; Mayrhofer, K. J. J.; Hassel, A. W.; Widdel, F.; Stratmann, M. *Corros. Sci.* **2013**, *66*, 88−96.

(22) Enning, D.; Venzlaff, H.; Garrelfs, J.; Dinh, H. T.; Meyer, V.; Mayrhofer, K.; Hassel, A. W.; Stratmann, M.; Widdel, F. *Environ. Microbiol.* **2012**, *14*, 1772−1787.

(23) Enning, D.; Garrelfs, J. *Appl. Environ. Microb.* **2014**, *80*, 1226−1236.

(24) de Médicis, R. *Science* **1970**, *170*, 1191−1192.

(25) Tang, J.; Shao, Y.; Guo, J.; Zhang, T.; Meng, G.; Wang, F. *Corros. Sci.* **2010**, *52*, 2050−2058.

DOI: 10.1021/acs.cgd.7b01013
Cryst. Growth Des. XXXX, XXX, XXX−XXX

(26) Muyzer, G.; Stams, A. J. M. *Nat. Rev. Microbiol.* **2008**, *6*, 441−454.
(27) Dinh, H. T.; Kuever, J.; Mußmann, M.; Hassel, A. W.; Stratmann, M.; Widdel, F. *Nature* **2004**, *427*, 829−832.
(28) Rickard, D.; Luther, G. W. *Chem. Rev.* **2007**, *107*, 514−562.
(29) Wiberg, E.; Wiberg, N. In *Inorganic Chemistry*; Academic Press: London, UK, 2001; pp 1451−1452.
(30) Herbert, F. W. PhD thesis; Massachusetts Institute of Technology: Cambridge, MA, 2015; Chapter 1, pp 14−20.
(31) Sun, W.; Nesic, S. *Corrosion* **2009**, *65*, 291−307.
(32) Smith, S. N.; Brown, B.; Sun, W. In *Corrosion 2011 Conference and Expo*; NACE International: Houston, TX, 2011; Paper No. 11081, pp 4056−4073.
(33) Bai, P.; Zheng, S.; Chen, C.; Zhao, H. *Cryst. Growth Des.* **2014**, *14*, 4295−4302.
(34) Shoesmith, D. W.; Bailey, M. G.; Ikeda, B. *Electrochim. Acta* **1978**, *23*, 1329−1339.
(35) Shoesmith, D. W.; Taylor, P.; Bailey, M. G.; Owen, D. G. *J. Electrochem. Soc.* **1980**, *127*, 1007−1015.
(36) Hartle, M. D.; Pluth, M. D. *Chem. Soc. Rev.* **2016**, *45*, 6108−6117.
(37) Cline, J. D. *Limnol. Oceanogr.* **1969**, *14*, 454−458.
(38) ICDD *Power Diffraction File Inorganc and Organic Data Book*; International Center for Diffraction Data: Newton Square, PA, 2013.
(39) Roine, A. *HSC Chemistry Database 5.11*; Outokumpu Research: Helsinki, Finland, 2002.
(40) Perez, N. In *Electrochemistry and Corrosion Science*; Springer International Publishing: Switzerland, 2004; Chapter 5, pp 155−166.
(41) Lewis, A. E. *Hydrometallurgy* **2010**, *104*, 222−234.
(42) Gevantman, L. H. In *CRC Handbook of Chemistry and Physics*, 94th ed.; Lide, D. R., Haynes, W. M., Eds.; CRC Press: Boca Raton, FL, 2013.
(43) Rickard, D. *Geochim. Cosmochim. Acta* **1995**, *59*, 4367−4379.
(44) Murowchick, J. B.; Barnes, H. L. *Am. Mineral.* **1986**, *71*, 1243−1246.
(45) Bourdoiseau, J. A.; Jeannin, M.; Sabot, R.; Rémazeilles, C.; Refait, P. *Corros. Sci.* **2008**, *50*, 3247−3255.
(46) Caracas, R.; Bobocioiu, E. *EMU Notes Mineralog.* **2012**, *12*, 173−191.
(47) Osadchii, E. G.; Gorbaty, Y. E. *Geochim. Cosmochim. Acta* **2010**, *74*, 568−573.
(48) Dandekar, P.; Kuvadia, Z. B.; Doherty, M. F. *Annu. Rev. Mater. Res.* **2013**, *43*, 359−386.
(49) Scharifker, B. R.; Mostany, J. In *Encyclopedia of Electrochemistry*; John Wiley & Sons: Hoboken, NJ, 2007; Chapter 5, pp 512−539.
(50) Gao, S.; Jin, P.; Brown, B.; Young, D.; Nesic, S.; Singer, M. *Corrosion* **2017**, *73*, 915−926.

DOI: 10.1021/acs.cgd.7b01013
Cryst. Growth Des. XXXX, XXX, XXX−XXX